molecules

MDPI

Article

Adsorption Features of Tetrahalomethanes (CX_4; X = F, Cl, and Br) on β_{12} Borophene and Pristine Graphene Nanosheets: A Comparative DFT Study

Mahmoud A. A. Ibrahim [1,2,*], Amna H. M. Mahmoud [1], Nayra A. M. Moussa [1], Gamal A. H. Mekhemer [1], Shaban R. M. Sayed [3], Muhammad Naeem Ahmed [4], Mohamed K. Abd El-Rahman [5], Eslam Dabbish [6] and Tamer Shoeib [6,*]

1 Computational Chemistry Laboratory, Chemistry Department, Faculty of Science, Minia University, Minia 61519, Egypt; a.mahmoud@compchem.net (A.H.M.M.); n.moussa@compchem.net (N.A.M.M.); gmekhemer@mu.edu.eg (G.A.H.M.)
2 School of Health Sciences, University of KwaZulu-Natal, Westville Campus, Durban 4000, South Africa
3 Department of Botany and Microbiology, College of Science, King Saud University, P.O. Box 2455, Riyadh 11451, Saudi Arabia; shmohamed@ksu.edu.sa
4 Department of Chemistry, The University of Azad Jammu and Kashmir, Muzaffarabad 13100, Pakistan; drnaeem@ajku.edu.pk
5 Department of Chemistry and Chemical Biology, Harvard University, 12 Oxford Street, Cambridge, MA 02138, USA; kabdelazim@gmwgroup.harvard.edu
6 Department of Chemistry, The American University in Cairo, New Cairo 11835, Egypt; emoustafa@aucegypt.edu
* Correspondence: m.ibrahim@compchem.net (M.A.A.I.); t.shoeib@aucegypt.edu (T.S.)

check for updates

Citation: Ibrahim, M.A.A.; Mahmoud, A.H.M.; Moussa, N.A.M.; Mekhemer, G.A.H.; Sayed, S.R.M.; Ahmed, M.N.; Abd El-Rahman, M.K.; Dabbish, E.; Shoeib, T. Adsorption Features of Tetrahalomethanes (CX_4; X = F, Cl, and Br) on β_{12} Borophene and Pristine Graphene Nanosheets: A Comparative DFT Study. *Molecules* **2023**, *28*, 5476. https://doi.org/10.3390/molecules28145476

Academic Editors: Tian Wang, Cheng Zhong, Tianyuan Zhang and Xiaohua Wang

Received: 21 June 2023
Revised: 14 July 2023
Accepted: 14 July 2023
Published: 18 July 2023

Abstract: The potentiality of the β_{12} borophene (β_{12}) and pristine graphene (GN) nanosheets to adsorb tetrahalomethanes (CX_4; X = F, Cl, and Br) were investigated using density functional theory (DFT) methods. To provide a thorough understanding of the adsorption process, tetrel ($XC\text{-}X_3\cdots\beta_{12}$/GN)- and halogen ($X_3C\text{-}X\cdots\beta_{12}$/GN)-oriented configurations were characterized at various adsorption sites. According to the energetic manifestations, the adsorption process of the $CX_4\cdots\beta_{12}$/GN complexes within the tetrel-oriented configuration led to more desirable negative adsorption energy (E_{ads}) values than that within the halogen-oriented analogs. Numerically, E_{ads} values of the $CBr_4\cdots Br1@\beta_{12}$ and T@GN complexes within tetrel-/halogen-oriented configurations were −12.33/−8.91 and −10.03/−6.00 kcal/mol, respectively. Frontier molecular orbital (FMO) results exhibited changes in the E_{HOMO}, E_{LUMO}, and E_{gap} values of the pure β_{12} and GN nanosheets following the adsorption of CX_4 molecules. Bader charge transfer findings outlined the electron-donating property for the CX_4 molecules after adsorbing on the β_{12} and GN nanosheets within the two modeled configurations, except the adsorbed CBr_4 molecule on the GN sheet within the tetrel-oriented configuration. Following the adsorption process, new bands and peaks were observed in the band structure and density of state (DOS) plots, respectively, with a larger number in the case of the tetrel-oriented configuration than in the halogen-oriented one. According to the solvent effect affirmations, adsorption energies of the $CX_4\cdots\beta_{12}$/GN complexes increased in the presence of a water medium. The results of this study will serve as a focal point for experimentalists to better comprehend the adsorption behavior of β_{12} and GN nanosheets toward small toxic molecules.

Keywords: tetrahalomethanes; graphene nanosheet; borophene nanosheet; DFT

1. Introduction

Two-dimensional (2D) nanomaterials have recently been of universal interest owing to their outstanding chemical and physical properties [1–4]. As a premier developed 2D material, pristine graphene (GN) was regarded as the most intriguing star in the realm of materials science [5–11]. GN-based materials were denoted with unique features, including

a high specific surface area [12], quantum Hall effect [13], high thermal conductivity [14], and ambipolar electric field effect [15]. Such properties shed light on their vast-ranging applications, like energy storage [16,17], drug delivery [18–21], spintronics [22], and catalysis [23]. Because of their low electronic noise, GN-based materials were also announced as an appealing candidate for adsorbing chemical systems [6,24].

Following the astonishing discovery of GN sheets, considerable research has been directed to develop various 2D materials, including antimonene [25], hexagonal boron nitride (h-BN) [26], bismuthine [27], silicene [28,29], and borophene [30,31]. In the parallel area, borophene, a 2D boron sheet, was announced with extraordinary properties, like electron mobility, anisotropic properties, superconductivity, and its phonon-mediated form [32–34]. Borophene was successfully fabricated on a single surface of Ag(111) under ultrahigh-vacuum conditions [30,31]. Different borophene phases were observed at various deposition temperatures using a high-resolution scanning tunneling microscope (STM), such as the striped, β_{12}, and χ_3 phases [31]. The puckered shape and metallic characteristics of the striped phase led to its utility in various potential applications for metal ion storage and electric conduction [35]. Compared with the striped phase, the preferable stability of the β_{12} and the χ_3 phases, with planar shapes having hexagonal and triangular vacancies, was demonstrated [36,37]. Because of its structure with a hexagonal vacancy, borophene was utilized in adsorbing gas molecules [10,38–40].

An upsurge in interest has recently been oriented toward investigating the utility of borophene and GN in the detection of gas molecules, like NO, CO, NO_2, CO_2, CS_2, and NH_3 molecules [40–43]. Halomethanes are known for being toxic molecules [44–46]; however, scant attention has been directed toward exploring novel nanomaterials for adsorbing them. Using density functional theory (DFT), the adsorption of tetrahalomethanes CX_4 (X = F, Cl, and Br) was studied on carbon nanotubes [47] and GN nanosheets [48]. Nevertheless, no comparative study provided a full insight into the adsorption process of the tetrahalomethanes via all their possible oriented configurations on the surface of the borophene and GN nanosheets.

Herein, the adsorption features of tetrahalomethanes (CX_4, where X = F, Cl, and Br) on the β_{12} borophene (β_{12}) nanosheet were unveiled and compared with those with the utilization of the GN nanosheet as the starting 2D nanomaterial. The $CX_4 \cdots \beta_{12}$/GN complexes were selectively studied within tetrel (XC-X_3)- and halogen (X_3C-X)-oriented configurations (Figure 1) using various density functional theory (DFT) method. Initially, geometry relaxation of the potential binding modes of the two suggested configurations and their corresponding adsorption energies were first carried out. Additionally, to assess the change in the electronic characteristics of the studied 2D nanosheets following the adsorption of the CX_4 molecules, Bader charge, electronic band structure, and density of state (DOS) calculations were conducted. Further, the solvent effect on the adsorption energy of the studied complexes was evaluated. The obtained results would be an informative base for the utilization of the β_{12} and GN in adsorbing small molecules, such as tetrahalomethanes.

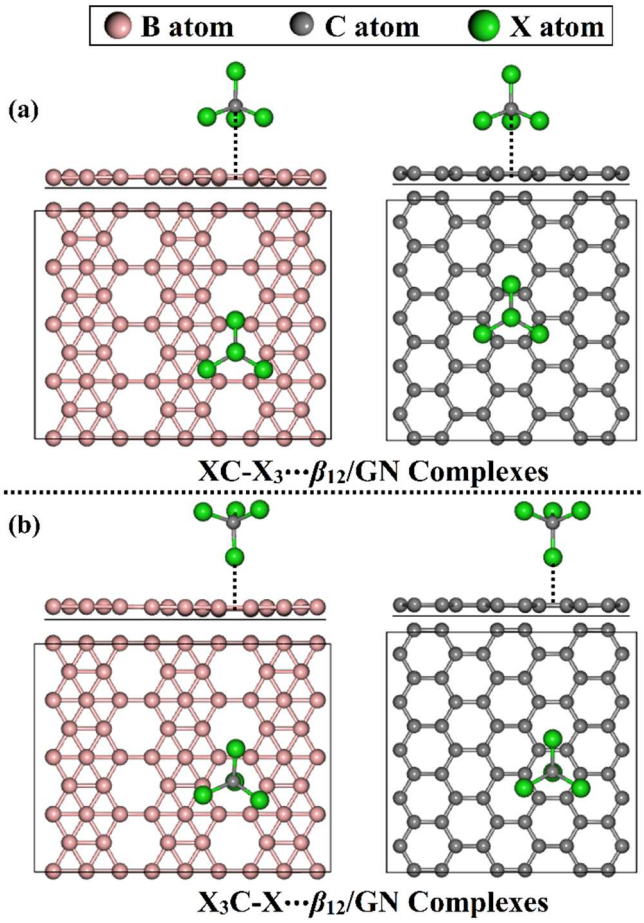

Figure 1. Side and top representations of the $CX_4 \cdots \beta_{12}$/GN complexes (where X = F, Cl, and Br) within (**a**) tetrel ($XC\text{-}X_3$)- and (**b**) halogen ($X_3C\text{-}X$)-oriented configurations.

2. Results and Discussion

2.1. Geometric Structures

β_{12} and GN structures were modeled and relaxed before the adsorption process of the tetrahalomethanes. The optimized β_{12} and GN structures are presented in Figure 2. The obtained equilibrium lattice constants for the primitive cells of the β_{12} nanosheet were a = 5.06 Å and b = 2.93 Å. For the GN nanosheet, the equilibrium lattice constants were $a = b$ = 2.47 Å. The current findings are consistent with earlier research [30,49,50]. On the β_{12} optimized structure, six adsorption sites were detected, comprising three top (T1, T2, and T3), two bridge (Br1 and Br2), and one hollow (H) sites (Figure 2). Looking at the GN surface, three adsorption sites, namely the top (T), bridge (Br), and hollow (H) sites, were noticed (Figure 2).

2.2. Adsorption Energy Calculations

The adsorption of tetrahalomethanes CX_4 (where X = F, Cl, and Br) on the surfaces of β_{12} and GN was investigated at different adsorption sites within the tetrel ($XC\text{-}X_3$)- and halogen ($X_3C\text{-}X$)-oriented configurations. The adsorption energies and the corresponding equilibrium distances of all relaxed $CX_4 \cdots \beta_{12}$/GN complexes were calculated and are summarized in Table 1. Figure S1 illustrates all relaxed complexes. The relaxed $CX_4 \cdots \beta_{12}$/GN complexes at the most energetically preferable adsorption sites are displayed in Figure 3.

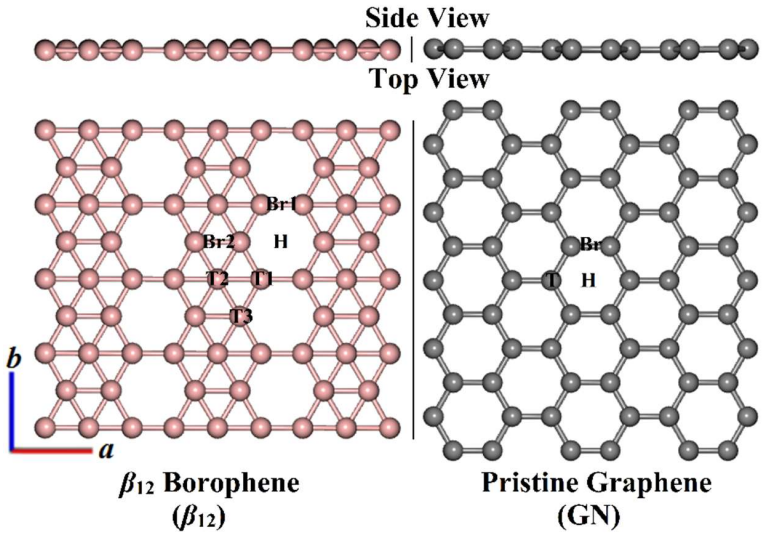

Figure 2. Side and top perspectives of the relaxed structures of 3 × 4 × 1 β_{12} borophene (β_{12}) and 6 × 5 × 1 pristine graphene (GN) with the studied adsorption sites. The boron and carbon atoms are represented by pink and gray colors, respectively. Top, hollow, and bridge adsorption sites are referred to as T, H, and Br, respectively.

Table 1. Adsorption energies (E_{ads}, kcal/mol) and equilibrium distances (d, Å) of the relaxed $CX_4 \cdots \beta_{12}$/GN complexes (where X = F, Cl, and Br) at all possible sites within the tetrel (XC-X_3)- and halogen (X_3C-X)-oriented configurations. Charge transfer difference (Q_t, *e*) for the 2D nanosheets before and after the adsorption process.

2D Nanosheets	Adsorption Site [a]	X = F			X = Cl			X = Br		
		E_{ads} (kcal/mol)	d (Å)	Q_t [b] (*e*)	E_{ads} (kcal/mol)	d (Å)	Q_t [b] (*e*)	E_{ads} (kcal/mol)	d (Å)	Q_t [b] (*e*)
Tetrel-oriented configuration										
β_{12}	T1	−4.42	3.69	−0.0309	−7.47	4.09	−0.0275	−11.45	4.14	−0.0231
	T2	−4.25	3.72	−0.0289	−7.69	4.06	−0.0230	−11.42	4.13	−0.0080
	T3	−4.14	3.68	−0.0309	−7.22	4.11	−0.0275	−11.07	4.17	−0.0215
	H	−4.39	3.65	−0.0306	−7.21	4.07	−0.0219	−11.15	4.13	−0.0115
	Br1	−4.46	3.67	−0.0313	−7.74	4.05	−0.0283	−12.33	4.11	−0.0263
	Br2	−4.14	3.74	−0.0291	−7.15	4.12	−0.0269	−11.03	4.18	−0.0175
GN	T	−4.66	3.50	−0.0175	−7.32	3.93	−0.0072	−10.03	4.07	0.0036
	Br	−4.36	3.57	−0.0177	−6.82	4.02	−0.0051	−9.49	4.13	0.0023
	H	−4.12	3.63	−0.0168	−6.57	4.06	−0.0025	−9.43	4.13	0.0070
Halogen-oriented configuration										
β_{12}	T1	−2.54	3.10	−0.0164	−5.14	3.16	−0.0410	−8.65	3.10	−0.0654
	T2	−2.62	3.12	−0.0149	−4.33	3.26	−0.0254	−6.72	3.21	−0.0291
	T3	−2.63	3.06	−0.0167	−4.97	3.17	−0.0366	--- [c]	--- [c]	--- [c]
	H	−2.71	2.93	−0.0185	−5.58	3.02	−0.0321	−9.00	2.98	−0.0424
	Br1	−2.46	3.11	−0.0165	−5.25	3.13	−0.0413	−8.91	2.98	−0.0697
	Br2	−2.69	3.05	−0.0163	−4.26	3.26	−0.0258	−6.37	3.24	−0.0317
GN	T	−2.46	3.00	−0.0095	−4.22	3.16	−0.0149	−6.00	3.17	−0.0196
	Br	−2.47	2.99	−0.0094	−4.18	3.17	−0.0152	−5.93	3.18	−0.0174
	H	−2.61	2.89	−0.0093	−3.99	3.18	−0.0093	−5.54	3.23	−0.0086

[a] All adsorption sites on the investigated 2D nanosheets are depicted in Figure 2. [b] Q_t was calculated based on Equation (3). [c] Desired configuration was not observed after geometry relaxation (see Figure S1).

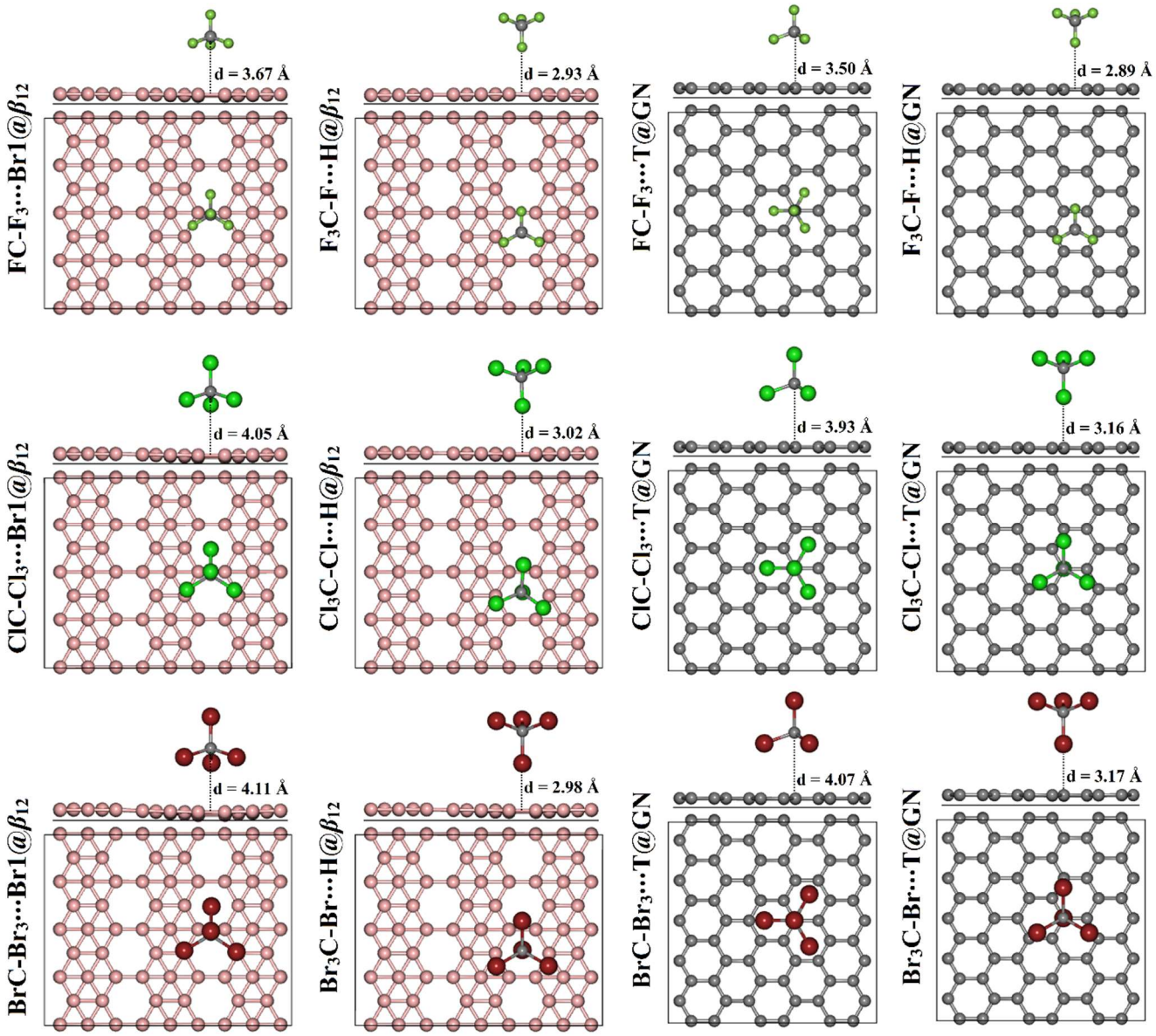

Figure 3. Side and top perspectives of the relaxed $CX_4 \cdots \beta_{12}$/GN complexes (where X = F, Cl, and Br) at the most preferable adsorption sites within tetrel ($XC\text{-}X_3$)- and halogen ($X_3C\text{-}X$)-oriented configurations. Equilibrium distances (d) are in Å. The boron, carbon, fluorine, chlorine, and bromine atoms are defined by pink, gray, pale green, green, and red colors, respectively.

For the adsorption process of the CX_4 on the β_{12} nanosheet within the tetrel-oriented configuration, the $BrC\text{-}Br_3 \cdots \beta_{12}$ complexes had the most significant E_{ads} values, followed by the $ClC\text{-}Cl_3 \cdots \beta_{12}$, then the $FC\text{-}F_3 \cdots \beta_{12}$ complexes (Table 1). Numerically, the E_{ads} of the $BrC\text{-}Br_3 \cdots$, $ClC\text{-}Cl_3 \cdots$, and $FC\text{-}F_3 \cdots Br1@\beta_{12}$ complexes were −12.33, −7.74, and −4.46 kcal/mol, respectively. These findings were in accord with a prior study, indicating that the adsorption energies increased with the increasing atomic size of the halogen atom (decreasing the electronegativity of the halogen atom) [51]. It is worth noting that the most preferred complex was the $BrC\text{-}Br_3 \cdots Br1@\beta_{12}$ complex, with an E_{ads} value of −12.33 kcal/mol and an equilibrium distance of 4.11 Å. In line with the tetrel-oriented configuration, energetic manifestations of the halogen-oriented complexes (i.e., $X_3C\text{-}X \cdots \beta_{12}$) showed the existence of a direct correlation between the adsorption energy and the atomic size of the halogen atom. Apparently, the $H@\beta_{12}$ site was the most appropriate adsorption site for adsorbing the $X_3C\text{-}X$ molecules in the halogen-oriented configuration. Moreover, the $Br_3C\text{-}Br \cdots H@\beta_{12}$

complex had the most prominent E_{ads} with a value of −9.00 kcal/mol at an equilibrium distance of 2.98 Å. The efficiency of the β_{12} nanosheet to adsorb the CX_4 molecules was more significant in the tetrel-oriented configuration than in the halogen-oriented one (Table 1). For instance, the E_{ads} values of the adsorption of the CBr_4 at the Br1@β_{12} site were −12.33 and −8.91 kcal/mol in the tetrel- and halogen-oriented configurations, respectively.

For the adsorption of CX_4 on the GN nanosheet, all complexes showed negative E_{ads} values, confirming the occurrence of the adsorption process. Similar to the $CX_4 \cdots \beta_{12}$ complexes, the preferentiality of the adsorption process of the CX_4 molecules on the GN nanosheet increased upon the following order X = F < Cl < Br. Obviously, the T@GN site had the highest tendency for adsorbing the studied tetrahalomethanes on the GN sheet, exhibiting significant E_{ads} values. Numerically, the ClC-$Cl_3\cdots$ and Cl_3C-Cl···T@GN complexes had E_{ads} values of −7.32 and −4.22 kcal/mol, respectively (Table 1).

For all $CX_4 \cdots \beta_{12}$/GN complexes, the obtained E_{ads} values ranged from −2.46 to −12.33 kcal/mol, demonstrating the occurrence of physisorption processes. The latter observation was in line with the literature, which reported the adsorption energy of $CH_4\cdots$, $CF_4\cdots$, and $CCl_4\cdots$GN complexes with values of −1.61, −3.46, and −8.99 kcal/mol, respectively [52]. While the adsorption of the CH_4 molecule on the borophene nanosheet exhibited a small E_{ads} value of −2.54 kcal/mol and was accordingly documented as a physisorption process [53]. For a given type of halogen, the β_{12} nanosheet showed more affinity to adsorb the CX_4 molecules than the GN nanosheet, which can be attributed to the lower electronegativity of boron relative to carbon and, hence, a lower electronegativity difference compared with that of the halogen.

Besides, the adsorption of the tetrahalomethanes became more favorable by decreasing the electronegativity of the halogens in the following order $CF_4\cdots$ > $CCl_4\cdots$ > $CBr_4 \cdots \beta_{12}$/GN, which was accompanied by a lower electronegativity difference in the case of boron compared with carbon atoms. The favorability of the adsorption process within the tetrel-oriented configuration might be attributed to the contribution of the three halogen atoms of XC-X_3 molecules to the overall interaction.

2.3. Frontier Molecular Orbital (FMO) Calculations

In order to comprehend the effect of the adsorption process on the electronic characteristics of the examined systems, the energies of the highest occupied molecular orbitals (E_{HOMO}), the lowest unoccupied molecular orbitals (E_{LUMO}), and the energy gap (E_{gap}) values were assessed. Table 2 shows data of the E_{HOMO}, E_{LUMO}, and E_{gap} values of the investigated systems before and following the adsorption process.

According to the data in Table 2, notable differences in the E_{HOMO}, E_{LUMO}, and E_{gap} values were observed for the studied systems before and following the adsorption process. For instance, in the tetrel-oriented configuration, the E_{HOMO} value of the BrC-$Br_3\cdots$Br1@β_{12} complex was −2.544 eV, whereas the pure β_{12} nanosheet had an E_{HOMO} value of −2.875 eV (Table 2). Moreover, the E_{gap} values of all CX_4 molecules, β_{12}, and GN nanosheets were altered, confirming the occurrence of adsorption processes. For example, the pure β_{12} nanosheet had an E_{gap} value of −0.626 eV that was changed to −0.602 eV after the adsorption process within the BrC-$Br_3\cdots$Br1@β_{12} complex (Table 2).

2.4. Charge Transfer Calculations

The Bader charge method is a reliable appliance for determining the charge transfer over the adsorption process [54,55]. The transferred charge between the CX_4 molecules and the 2D nanosheets within all the studied complexes was evaluated in terms of the charge transfer difference (Q_t) values (Table 1). The Q_t values with negative signs remarked that the charge was shifted from the CX_4 molecules towards the β_{12} and GN nanosheets, and vice versa was true for the positive Q_t values.

Table 2. The energies of the highest occupied molecular orbitals (E_{HOMO}, eV), the lowest unoccupied molecular orbitals (E_{LUMO}, eV), and the energy gap (E_{gap}, eV) of the CX_4 molecules and the β_{12}/GN nanosheets before and after the adsorption process.

Complex [a]	E_{HOMO} (eV)	E_{LUMO} (eV)	E_{gap} (eV)
Isolated systems			
GN Nanosheet	−2.354	−2.343	0.011
β_{12} Nanosheet	−2.875	−3.501	−0.626
CF_4	−10.333	−0.477	9.855
CCl_4	−7.416	−2.680	4.735
CBr_4	−6.644	−3.394	3.250
Tetrel-oriented Configuration			
FC-F_3···Br1@β_{12}	−2.734	−3.358	−0.625
ClC-Cl_3···Br1@β_{12}	−2.602	−3.217	−0.615
BrC-Br_3···Br1@β_{12}	−2.544	−3.146	−0.602
FC-F_3···T@GN	−2.202	−2.191	0.0104
ClC-Cl_3···T@GN	−2.064	−2.054	0.0107
BrC-Br_3···T@GN	−2.010	−1.999	0.0108
Halogen-oriented Configuration			
F_3C-F···H@β_{12}	−2.737	−3.364	−0.627
Cl_3C-Cl···H@β_{12}	−2.612	−3.237	−0.626
Br_3C-Br···H@β_{12}	−2.564	−3.190	−0.626
F_3C-F···H@GN	−2.200	−2.190	0.0104
Cl_3C-Cl···T@GN	−2.066	−2.056	0.0104
Br_3C-Br···T@GN	−2.021	−2.010	0.0105

[a] Structures of the most stable relaxed CX_4···β_{12}/GN complexes within both configurations are presented in Figure 3.

Table 1 shows Q_t values with a negative sign for the CX_4···β_{12} complexes, demonstrating the ability of the inspected tetrahalomethanes to donate electrons to the β_{12} nanosheets within the tetrel- and halogen-oriented configurations. Notably, the Q_t values of the CX_4···β_{12} complexes within the halogen-oriented configuration generally decreased as the adsorption energies decreased (i.e., in the order CBr_4··· > $CC1_4$··· > CF_4···β_{12}). For instance, the Q_t values of the Br_3C-Br···, Cl_3C-Cl···, and F_3C-F···T1@β_{12} complexes were −0.0654, −0.0410, and −0.0164 *e*, respectively. The reversed trend was noticed for the complexes within the tetrel-oriented configuration, outlining the noticeable contributions of the three coplanar halogen atoms to the adsorption process. For example, the Q_t values for the CF_4···, CCl_4···, and CBr_4···Br1@β_{12} complexes within the tetrel-oriented configuration were −0.0313, −0.0283, and −0.0263 *e*, respectively.

The Q_t values of the CX_4···GN complexes within the tetrel- and halogen-oriented configurations showed similar trends to the CX_4···β_{12} complexes, except for the CBr_4···GN complexes within the former configuration that had positive Q_t values. For the latter complexes, the electron-accepting property increased in the following order, H@GN < Br@GN < T@GN adsorption sites, and was confirmed with positive Q_t values of 0.0070, 0.0023, and 0.0036 *e*, respectively.

Charge density difference ($\Delta\rho$) maps were generated in order to investigate the distribution of the charge within the relaxed CX_4···β_{12}/GN complexes at the most preferable adsorption sites, and the maps are provided in Figure 4. As demonstrated in Figure 4, the electron depletion and accumulation regions (i.e., cyan- and yellow-colored regions, respectively) revealed the distribution of the charge between the tetrahalomethanes and the investigated 2D nanosheets. Apparently, the most remarkable electron-accumulated

region was observed for the $CBr_4 \cdots \beta_{12}$/GN complexes, demonstrating the further ability of CBr_4 molecules to be adsorbed on the studied 2D nanosheets among tetrahalomethane analogs (Figure 4).

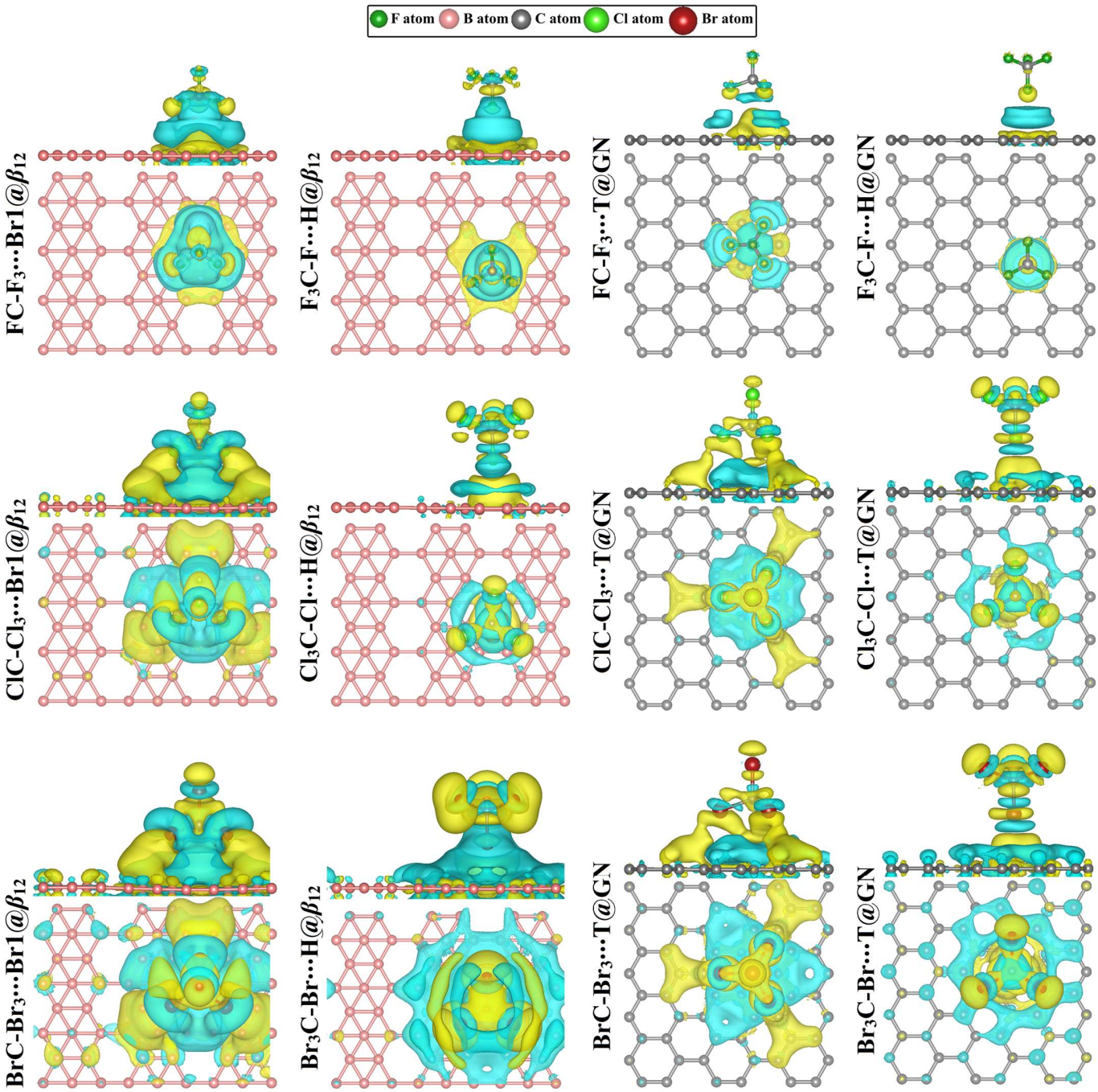

Figure 4. Charge density difference ($\Delta\rho$) maps of the relaxed $CX_4 \cdots \beta_{12}$/GN complexes (where X = F, Cl, and Br) at the most preferable adsorption sites within tetrel (XC-X_3)- and halogen (X_3C-X)-oriented configurations. Regions with cyan and yellow colors refer to depletion (negative) and accumulation (positive) charges, respectively. The isosurface values for the $CX_4 \cdots \beta_{12}$ and $\cdots$GN were set to be 3.08×10^{-5} and 5.0×10^{-5} $e/\text{Å}^3$, respectively.

Overall, the negative Q_t values confirmed that all the CX_4 molecules had an electron-donating character except for the $CBr_4 \cdots$GN complexes within the tetrel-oriented configuration. According to the Q_t values, the amount of charge transferred from the tetrahalomethanes to the β_{12} nanosheet was more significant than that of the GN nanosheet,

which was in line with the adsorption energy values. Based on $\Delta\rho$ maps, it was observed that the amount of the distribution charge area (colored area) increased as the electronegativity of the halogen atom decreased. For instance, the size of the distribution charge area increased as the atomic size of the halogen atom increased in the order FC-F_3··· < ClC-Cl_3··· < BrC-Br_3···Br1@β_{12} complexes.

Given that the Q_t values of the CX_4···β_{12}/GN complexes within the halogen-oriented configuration generally decreased as the adsorption energies decreased, while the reversed trend was noticed for the complexes within the tetrel-oriented configuration. This implies that the halogen orientation relies on a more localized charge transfer and electronegativity difference during the binding mechanism, while the tetrel orientation is accompanied by a more distributed charge transfer binding that is more significant with large-sized bromine atoms.

2.5. Band Structure Calculations

To ascertain the impact of the adsorption of the CX_4 molecules on the electronic properties of the β_{12} and GN nanosheets, band structure analysis was carried out for the pure and combined 2D nanosheets. Using PBE functional along the high-symmetry paths of the Brillouin zone, band structures were extracted. The Γ-Y-S-X-Γ path was chosen for the β_{12} nanosheet, and the Y-S-X-Γ-Y path was selected for the GN nanosheet. The band structures of the pure 2D nanosheets are demonstrated in Figure S2.

Looking at Figure S2, a metallic character of the pure β_{12} surface was noted by several bands, which crossed the Fermi level along the high-symmetry path. For the pure GN surface, the existence of the Dirac point at the Fermi level announced its semiconducting property.

Band structures of the relaxed CX_4···β_{12}/GN complexes at the most preferable adsorption sites are plotted in Figure 5. After the adsorption process, slight differences were noticed in the electronic band structures of the pure nanosheets, outlining the physisorption process of tetrahalomethanes on the pure nanosheets (Figure 5).

For the adsorption of CF_4 molecules, insignificant changes were denoted in the electronic band structures of the β_{12} nanosheet. Upon adsorbing CCl_4 and CBr_4 molecules, further new bands appeared in the band structures of the combined nanosheets compared with the pure analogs. Such new bands remarked the adsorption of the CCl_4 and CBr_4 molecules on the β_{12} nanosheet. Illustratively, the CBr_4···β_{12} complexes displayed a new conduction band at 1.35 eV and new valence bands at −0.60 and −2.00 eV. It was also observed that the bands shifted towards the Fermi level in the case of the complexes within the tetrel-oriented configuration more than the halogen-oriented analog. For instance, the adsorption of CCl_4 at the Br1@β_{12} and H@β_{12} within the tetrel- and halogen-oriented configurations led to the appearance of a conduction band at around 2.70 and 2.15 eV, respectively. This observation demonstrated the higher favorability of the adsorption process within the former configuration than the latter one.

Similar to the β_{12} nanosheet, the CF_4 molecules had a neglected effect on the band structure of the pure GN surface (Figure 5). Besides, the band structures of the CCl_4··· and CBr_4···GN complexes showed many new valence and conduction bands, confirming the higher potentiality of the GN nanosheet to adsorb these molecules compared with CF_4 molecules. For instance, in the CBr_4···GN complexes, a new conduction band appeared at 0.60 and 0.67 eV, respectively, while in the valence region, many valence bands appeared at −2.40 eV and then ranged from −2.62 to −2.65 eV (Figure 5). It can be seen that the valence and conduction bands in the CX_4···GN complexes shifted towards the Fermi level as the atomic size of the halogen atom increased, demonstrating a favorable adsorption process. For example, the valence band at around −2.55 eV in the FC-F_3···T@GN complex shifted to −2.60 eV in the ClC-Cl_3···T@GN complex, and then to −2.65 eV in the BrC-Br_3···T@GN complex (Figure 5).

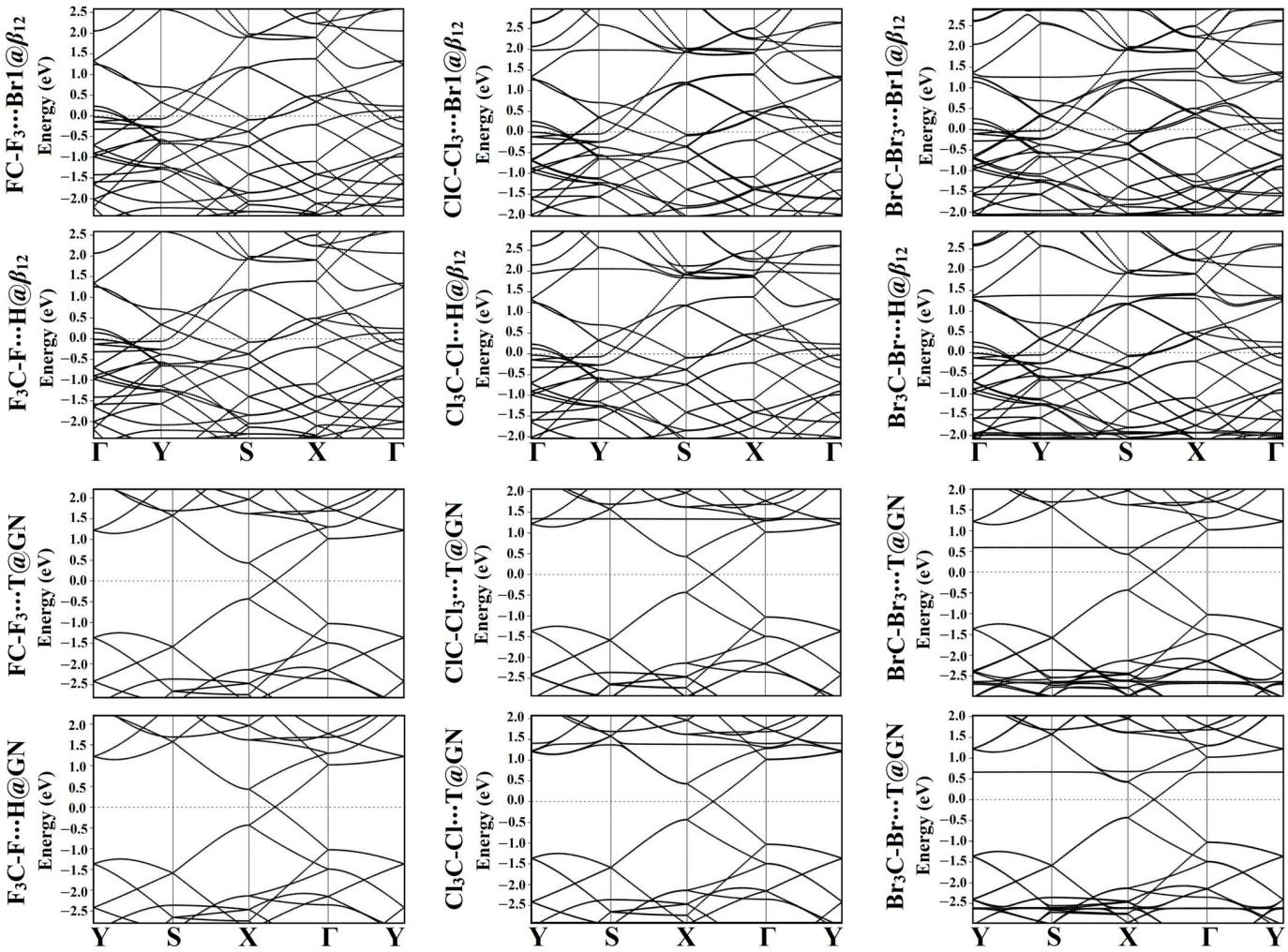

Figure 5. Band structure plots for the relaxed $CX_4 \cdots \beta_{12}$/GN complexes (where X = F, Cl, and Br) at the most preferable adsorption sites within tetrel (XC-X_3)- and halogen (X_3C-X)-oriented configurations. The Fermi energy was positioned at zero energy.

Summing up, the band structures of the β_{12} nanosheet demonstrated more new bands after adsorbing the CX_4 molecules than those of the GN nanosheet. The latter affirmation indicated the further desirability of the adsorption process on the β_{12} nanosheet than the GN nanosheet. The obtained findings were in line with the adsorption energy affirmations. The appearance of the new bands after the adsorption process indicated the overlap of the bands of the adsorbent and substrate, confirming the interaction between the CX_4 molecule and the studied 2D nanosheet. Further, the number of the new bands increased as the electronegativity of the halogen atom decreased. Illustratively, the $CBr_4 \cdots \beta_{12}$/GN complexes, which exhibited the highest negative adsorption energy, showed the largest number of new bands among the other complexes (Figure 5).

2.6. Density of State Calculations

The total density of state (TDOS), together with the projected density of state (PDOS), were extracted for pure and combined 2D nanosheets to truly comprehend the impact of the adsorption process on the electronic characteristics of the 2D nanosheets (Figure S3). TDOS and PDOS plots of the most favorable complexes are shown in Figure 6.

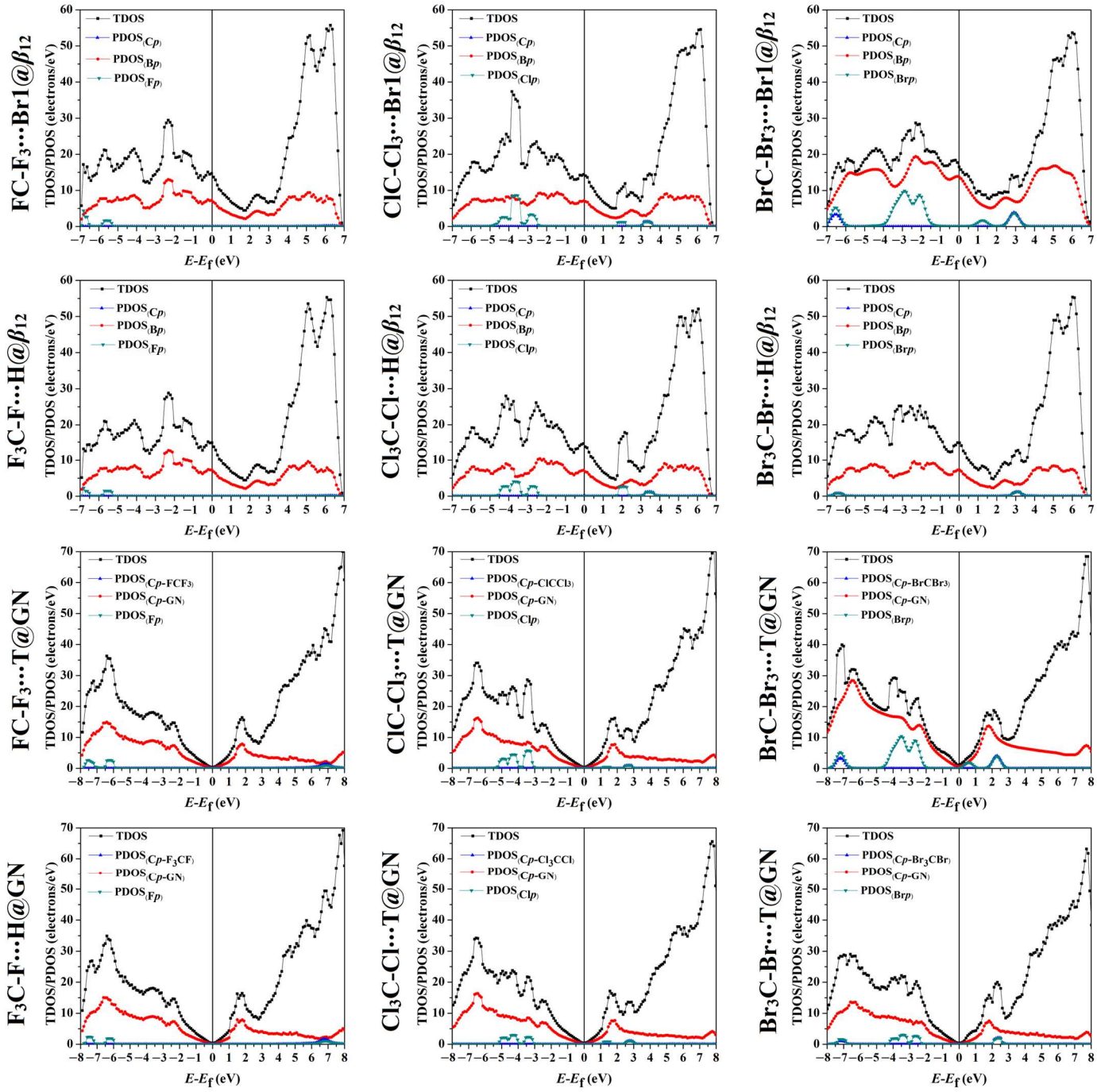

Figure 6. Total density of state (TDOS) plots for the relaxed $CX_4 \cdots \beta_{12}$/GN complexes (where X = F, Cl, and Br) at the most preferable adsorption sites within tetrel ($XC\text{-}X_3$)- and halogen ($X_3C\text{-}X$)-oriented configurations. The projected density of state (PDOS) with the contribution of B_p, $C_{p\text{-GN}}$, C_{P-CX_4}, and X_{P-CX_4}. The Fermi energy was set at zero energy.

The PDOS plots with the contribution of the *p*-orbital of B, C, and X atoms within the studied complexes were plotted in the energy range from −7.00 to 7.00 eV for β_{12} and from −8.00 to 8.00 eV for GN.

As shown in Figure 6, intense and feeble peaks were observed for the contributions of the PDOS of the X_{P-CX_4} and C_{P-CX_4}, respectively, to the TDOS of all the studied complexes. Accordingly, the halogens and carbon atoms of the CX_4 molecules exhibited major and minor roles within the adsorption process on the 2D nanosheets, respectively.

For example, the contribution of Cl_p to the $CCl_4 \cdots \beta_{12}$ and $\cdots$GN complexes within the tetrel-oriented configuration were found in the valence region ranging from −2.50 to −4.70 eV and −3.00 to −5.10 eV, respectively. At the same time, the contribution of Cl_p also appeared in the conduction regions from 1.70 to 2.30 eV and; 3.00 to 3.60 eV for the adsorption over the β_{12} nanosheet and between 2.50 and 3.00 eV for the GN analog. Within the halogen-oriented configuration, the Cl_p peaks of the adsorbed CCl_4 molecule on the β_{12} and GN nanosheets were noticed in the valence region between −2.40 and −4.50 eV and −3.00 and −5.00 eV, respectively. In the conduction region, the contribution of the Cl_p of the adsorbed CCl_4 molecule on the β_{12} and GN nanosheets were found in the energy ranges of 1.80–2.50 and 3.00–4.00 eV, and 1.10–1.60 and 2.50–3.10 eV, respectively.

Notably, hybridizations between the *p*-orbital of the 2D nanosheets and the *p*-orbital of the CX_4 molecules were also observed, revealing the occurrence of the adsorption process (Figure 6). For instance, an overlap between the $PDOS_{(Bp)}$ and the $PDOS_{(Clp)}$ appeared in the range from −3.50 to −3.90 eV in the $CCl_4 \cdots Br1@\beta_{12}$ complex within the tetrel-oriented configuration, affirming the ability of the β_{12} nanosheet to adsorb the CCl_4 molecule. The latter observation was consistent with the E_{ads} of the $CCl_4 \cdots Br1@\beta_{12}$ complex with a value of −7.74 kcal/mol (Table 1). While in the $CCl_4 \cdots H@\beta_{12}$ complex within the halogen-oriented configuration, a small overlap between the $PDOS_{(Bp)}$ of the β_{12} nanosheet and the $PDOS_{(Clp)}$ of the CCl_4 molecule was noticed in the conduction region from 1.80 to 2.20 eV. This finding was in agreement with the small E_{ads} value of −5.58 kcal/mol.

From the DOS outlines, halogens had the dominant role in the adsorption of the CX_4 molecules on the β_{12} and GN nanosheets within the modeled configurations. In line with the adsorption-energy and band structure findings, the DOS plots revealed the favorability of the β_{12} nanosheet over the GN analog to adsorb the tetrahalomethanes.

2.7. Solvent Effect Calculations

To speculate the effect of the solvent on the adsorption process within the $CX_4 \cdots \beta_{12}$/GN complexes, the adsorption energy was evaluated in the presence of a water solvent. Afterwards, the solvent effect ($E_{ads}^{solventeffect}$) energy was computed for the most preferable complexes as the difference between the adsorption energies of the water solvent and vacuum (see the Computational Methodology section for details). The obtained E_{ads}^{water} and $E_{ads}^{solventeffect}$ values are listed in Table 3.

According to the data presented in Table 3, the adsorption energies of the $CX_4 \cdots \beta_{12}$/GN complexes in the water medium showed higher negative values compared with those in a vacuum. For instance, the E_{ads}^{water} and E_{ads}^{vacuum} values of the $CBr_4 \cdots Br1@\beta_{12}$ complex within the tetrel-oriented configuration were −15.99 and −12.33 kcal/mol, respectively (Tables 1 and 3, respectively). Subsequently, $E_{ads}^{solvent\ effect}$ exhibited negative values, confirming the occurrence of the adsorption process in the water medium. As an illustration, the $E_{ads}^{solvent\ effect}$ value of the $CBr_4 \cdots Br1@\beta_{12}$ complex within the tetrel-oriented configuration was −3.66 kcal/mol. Similar to the energetic manifestation obtained in a vacuum, the more prevalent effect of the water solvent on the favorability of the adsorption process was ascribed to the complexes within the tetrel-oriented configuration compared with the halogen-oriented configuration. Numerically, as an example, the $E_{ads}^{solvent\ effect}$ values of the $CBr_4 \cdots Br1@\beta_{12}$ and $\cdots H@\beta_{12}$ complexes within the tetrel- and halogen-oriented configurations were −3.66 and −1.60 kcal/mol, respectively.

Table 3. Adsorption energy in the vacuum medium (E_{ads}^{vacuum}, kcal/mol), water medium (E_{ads}^{water}, kcal/mol), and the energy of the solvent effect ($E_{ads}^{solvent\ effect}$, kcal/mol) for the relaxed $CX_4 \cdots \beta_{12}$/GN complexes (where X = F, Cl, and Br) at the most preferable adsorption sites within the tetrel (XC-X_3)- and halogen (X_3C-X)-oriented configurations.

System [a]	E_{ads}^{vacuum} (kcal/mol)	E_{ads}^{water} (kcal/mol)	$E_{ads}^{solvent\ effect}$ [b] (kcal/mol)
Tetrel-oriented Configuration			
FC-F_3···Br1@β_{12}	−4.46	−6.91	−2.45
ClC-Cl_3···Br1@β_{12}	−7.74	−11.21	−3.47
BrC-Br_3···Br1@β_{12}	−12.33	−15.99	−3.66
FC-F_3···T@GN	−4.66	−7.14	−2.48
ClC-Cl_3···T@GN	−7.32	−10.99	−3.67
BrC-Br_3···T@GN	−10.03	−14.09	−4.06
Halogen-oriented Configuration			
F_3C-F···H@β_{12}	−2.71	−4.22	−1.51
ClC-Cl_3···H@β_{12}	−5.58	−7.26	−1.68
BrC-Br_3···H@β_{12}	−9.00	−10.60	−1.60
F_3C-F···H@GN	−2.61	−4.17	−1.56
Cl_3C-Cl···T@GN	−4.22	−5.98	−1.76
Br_3C-Br···T@GN	−6.00	−7.72	−1.72

[a] The structures of the relaxed complexes are depicted in Figure 3. [b] $E_{ads}^{solvent\ effect} = E_{ads}^{water} - E_{ads}^{vacuum}$.

3. Computational Methods

The density functional theory (DFT) method was applied for all calculations [56,57] via the Quantum ESPRESSO 6.4.1 package [58,59]. Based on the Perdew–Burke–Ernzerhof (PBE) scheme, the electron exchange-correlation function was conducted utilizing the generalized gradient approximation (GGA) [60]. To represent the electron–core interaction, the ultrasoft pseudopotential (USPP) was employed [61]. The van der Waals interactions for all the executed computations were taken into account using the Grimme-D2 method [62]. The utilized energy cutoff and charge density cutoff values were 50 and 500 Ry, respectively. The total energy and the atomic force convergence criteria were 1×10^{-5} eV and 1×10^{-4} eV/Å, respectively. Based on the Monkhorst-Pack mesh, the $6 \times 6 \times 1$ and $12 \times 12 \times 1$ *k*-points grids were adopted for the first Brillouin zone sampling within the geometry relaxation and density of state calculations, respectively. The convergence was enhanced using the Marzari–Vanderbilt smearing method [63]. For preventing image–image interaction, a vacuum thickness of 20 Å was added along the *z*-direction of the β_{12} and GN nanosheets.

To model the adsorption of the tetrahalomethanes (CX_4; X = F, Cl, and Br) on β_{12} and GN nanosheets, $3 \times 4 \times 1$ and $6 \times 5 \times 1$ supercells were constructed for β_{12} and GN nanosheets, respectively. Adsorption energies (E_{ads}) of the $CX_4 \cdots \beta_{12}$/GN complexes within tetrel (XC-X_3)- and halogen (X_3C-X)-oriented configurations were assessed as follows:

$$E_{ads} = E_{CX_4 \cdots 2D\ nanosheet} - \left(E_{CX_4} + E_{2D\ nanosheet}\right) \quad (1)$$

where $E_{CX_4 \cdots 2D\ nanosheet}$, E_{CX_4}, and $E_{2D\ nanosheet}$ are the energies of complex, tetrahalomethane, and 2D nanosheet, respectively. Frontier molecular orbital (FMO) calculations were carried out to gain a better understanding of the adsorption process of CX_4 molecules on the investigated 2D nanosheets. Within the FMO analyses, the energies of the highest occupied molecular orbitals (E_{HOMO}) and lowest unoccupied molecular orbitals (E_{LUMO}) for the most stable relaxed $CX_4 \cdots \beta_{12}$/GN complexes were computed. The energy gap (E_{gap}) was estimated according to the following equation:

$$E_{gap} = E_{LUMO} - E_{HOMO} \quad (2)$$

The charge transfer of the adsorbed CX_4 molecules was determined using the Bader charge method [55,64] based on the following equation:

$$Q_t = Q_{\text{combined 2D nanosheets}} - Q_{\text{isolated 2D nanosheets}} \quad (3)$$

where $Q_{\text{combined 2D nanosheets}}$ and $Q_{\text{isolated 2D nanosheets}}$ are the charges of the 2D nanosheets after adsorbing tetrahalomethanes and the charge of the isolated 2D nanosheets, respectively. The charge density difference ($\Delta\rho$) was plotted according to the following equation:

$$\Delta\rho = \rho_{CX_4\cdots\text{2D nanosheet}} - \rho_{CX_4} - \rho_{\text{2D nanosheet}} \quad (4)$$

where $\rho_{CX_4\cdots\text{2D nanosheet}}$, ρ_{CX_4}, and $\rho_{\text{2D nanosheet}}$ are the charge densities of complex, tetrahalomethane, and 2D nanosheet, respectively. VESTA 3 visualization software was invoked for generating the charge density plots [65]. To comprehend the influence of the adsorption process of the tetrahalomethanes on the electronic characteristics of the β_{12} and GN nanosheets, band structure and density of state (DOS) calculations were executed. For implicit water solvent calculations, the Environ code [66] of Quantum ESPRESSO was utilized with a dielectric constant of 78.3. The solvent effect on the adsorption energy of the studied complexes ($E_{ads}^{solvent\ effect}$) was computed according to the following equation:

$$E_{ads}^{solvent\ effect} = E_{ads}^{water} - E_{ads}^{vacuum} \quad (5)$$

where E_{ads}^{water} and E_{ads}^{vacuum} are the adsorption energies of the complex in water and vacuum media, respectively.

4. Conclusions

In the presented work, a DFT study was conducted to comparatively illustrate the adsorption features of tetrahalomethanes (CX_4, where X = F, Cl, and Br) on β_{12} borophene (β_{12}) and GN nanosheets. To attain a thorough investigation, geometry relaxation, adsorption energies, Bader charge, electronic band structures, and DOS computations were conducted for the adsorption of the CX_4 molecules on the studied 2D nanosheets within tetrel (XC-X_3)- and halogen (X_3C-X)-oriented configurations. From the energetic perspective, the adsorption of the CX_4 model on the β_{12} and GN nanosheets within the tetrel-oriented configuration was more desirable than that within the halogen-oriented configuration. Further favorability of the Br1@β_{12} and T@GN adsorption sites were announced toward adsorbing the CX_4 molecules within the tetrel-oriented configuration and showed the most significant E_{ads} for the CBr_4 molecule with values of −12.33 and −10.03 kcal/mol, respectively. According to the FMO results, the E_{HOMO}, E_{LUMO}, and E_{gap} values of the β_{12} and GN nanosheets were changed following the adsorption process. Based on the Bader charge results, the electron-donating characters for all the CX_4 molecules after adsorbing on the β_{12} and GN nanosheets within tetrel- and halogen-oriented configurations were illustrated, except the $CBr_4\cdots$GN complexes within the former configuration. In the latter complexes, the adsorbed CBr_4 molecule showed an electron-accepting property confirmed by the small positive Q_t values. From the band structure and DOS plots, new bands and peaks were observed, respectively, after the adsorption of CX_4 molecules on the 2D nanosheets, indicating the occurrence of the adsorption process. The energetic results are pertinent to the solvent effect demonstrated, that the presence of the water solvent led to more observable negative adsorption energies compared with the adsorption in a vacuum. The emerging findings would provide a foundation for any future consideration of β_{12} and GN nanosheets to adsorb small molecules.

Supplementary Materials: The following supporting information can be downloaded at: https://www.mdpi.com/article/10.3390/molecules28145476/s1, Figure S1: Side and top representations for the relaxed structures of the tetrel (XC-X_3)- and halogen (X_3C-X)-oriented configurations of the $CX_4\cdots\beta_{12}$/GN complexes (where X = F, Cl, and Br) at all the adsorption sites. Equilibrium distances (d) are given in Å; Figure S2: Electronic band structures of β_{12} and GN nanosheets along the high symmetry points of the Brillouin zone. The Fermi energy was set at zero energy, and the Dirac point is defined by the dotted circle; Figure S3: Total and projected density of state (TDOS/PDOS) plots for the pure surfaces of β_{12} and GN nanosheets, assuming Fermi level as the reference level. The dotted circle defines the Dirac point. The contributions of the *p*-orbital for boron (B) and carbon (C) atoms are represented by B_p and C_p, respectively.

Author Contributions: Conceptualization, M.A.A.I. and T.S.; Methodology, M.A.A.I., A.H.M.M. and T.S.; Software, M.A.A.I.; Formal analysis, A.H.M.M.; Investigation, A.H.M.M. and N.A.M.M.; Resources, M.A.A.I., S.R.M.S. and T.S.; Data curation, A.H.M.M.; Writing—original draft preparation, A.H.M.M.; Writing—review and editing, M.A.A.I., N.A.M.M., G.A.H.M., S.R.M.S., M.N.A., M.K.A.E.-R., E.D. and T.S.; Visualization, A.H.M.M.; Supervision, M.A.A.I. and G.A.H.M.; Project administration, M.A.A.I. and G.A.H.M. All authors have read and agreed to the published version of the manuscript.

Funding: This research received no external funding.

Institutional Review Board Statement: Not applicable.

Informed Consent Statement: Not applicable.

Data Availability Statement: Data will be made available on request.

Acknowledgments: The authors extend their appreciation to the Researchers Supporting Project number (RSPD2023R743), King Saud University, Riyadh, Saudi Arabia, for funding this work. The computational work was performed with resources provided by the Science and Technology Development Fund (STDF-Egypt, Grants Nos. 5480 and 7972), Bibliotheca Alexandrina (http://hpc.bibalex.org, accessed on 1 July 2023), and The American University in Cairo. Mahmoud A. A. Ibrahim extends his appreciation to the Academy of Scientific Research and Technology (ASRT, Egypt) for funding the Graduation Projects conducted at CompChem Lab, Egypt.

Conflicts of Interest: The authors declare no conflict of interest.

Sample Availability: Samples of the compounds (XYZ coordinates) are available from the authors.

References

1. Cao, M.S.; Wang, X.X.; Zhang, M.; Shu, J.C.; Cao, W.Q.; Yang, H.J.; Fang, X.Y.; Yuan, J. Electromagnetic response and energy conversion for functions and devices in low-dimensional materials. *Adv. Funct. Mater.* **2019**, *29*, 1807398. [CrossRef]
2. Tang, Q.; Zhou, Z. Graphene-analogous low-dimensional materials. *Prog. Mater. Sci.* **2013**, *58*, 1244–1315. [CrossRef]
3. Xia, F.; Wang, H.; Jia, Y. Rediscovering black phosphorus as an anisotropic layered material for optoelectronics and electronics. *Nat. Commun.* **2014**, *5*, 4458. [CrossRef] [PubMed]
4. Ibrahim, M.A.A.; Mahmoud, A.H.M.; Soliman, K.A.; Mekhemer, G.A.H.; Ahmed, M.N.; Shawky, A.M.; Abourehab, M.A.S.; Elkaeed, E.B.; Soliman, M.E.S.; Moussa, N.A.M. Borophene and pristine graphene 2D sheets as potential surfaces for the adsorption of electron-rich and electron-deficient pi-systems: A comparative DFT study. *Nanomaterials* **2022**, *12*, 1028. [CrossRef]
5. Novoselov, K.S.; Fal'ko, V.I.; Colombo, L.; Gellert, P.R.; Schwab, M.G.; Kim, K. A roadmap for graphene. *Nature* **2012**, *490*, 192–200. [CrossRef]
6. Schedin, F.; Geim, A.K.; Morozov, S.V.; Hill, E.W.; Blake, P.; Katsnelson, M.I.; Novoselov, K.S. Detection of individual gas molecules adsorbed on graphene. *Nat. Mater.* **2007**, *6*, 652–655. [CrossRef]
7. Leenaerts, O.; Partoens, B.; Peeters, F.M. Adsorption of H_2O, NH_3, CO, NO_2, and NO on graphene: A first-principles study. *Phys. Rev. B* **2008**, *77*, 125416–125421. [CrossRef]
8. Ren, Z.; Zhang, H.; Liu, N.; Lei, D.; Zhang, Q.; Su, T.; Wang, L.; Su, J.; Gao, Y. Self-powered 2D nanofluidic graphene pressure sensor with Serosa-Mimetic structure. *EcoMat* **2022**, *5*, e12299. [CrossRef]
9. Xiao, H.; Li, Y.; Chen, R.; Xie, T.; Xu, P.; Zhu, H.; He, J.; Zheng, W.; Huang, S. Integrative design of laser-induced graphene array with lithiophilic MnOx nanoparticles enables superior lithium metal batteries. *eScience* **2023**, 100134. [CrossRef]
10. Mujib, S.B.; Ren, Z.; Mukherjee, S.; Soares, D.M.; Singh, G. Design, characterization, and application of elemental 2D materials for electrochemical energy storage, sensing, and catalysis. *Mater. Adv.* **2020**, *1*, 2562–2591. [CrossRef]
11. Liu, X.M.; Xu, T.; Li, Y.L.; Zang, Z.G.; Peng, X.S.; Wei, H.Y.; Zha, W.Y.; Wang, F. Enhanced X-ray photon response in solution-synthesized CsPbBr3 nanoparticles wrapped by reduced graphene oxide. *Sol. Energy Mater. Sol. Cells* **2018**, *187*, 249–254. [CrossRef]
12. Rao, C.N.; Sood, A.K.; Subrahmanyam, K.S.; Govindaraj, A. Graphene: The new two-dimensional nanomaterial. *Angew. Chem. Int. Ed. Engl.* **2009**, *48*, 7752–7777. [CrossRef] [PubMed]
13. Zhang, Y.; Tan, Y.W.; Stormer, H.L.; Kim, P. Experimental observation of the quantum Hall effect and Berry's phase in graphene. *Nature* **2005**, *438*, 201–204. [CrossRef] [PubMed]
14. Balandin, A.A.; Ghosh, S.; Bao, W.; Calizo, I.; Teweldebrhan, D.; Miao, F.; Lau, C.N. Superior thermal conductivity of single-layer graphene. *Nano Lett.* **2008**, *8*, 902–907. [CrossRef]
15. Novoselov, K.S.; Geim, A.K.; Morozov, S.V.; Jiang, D.; Zhang, Y.; Dubonos, S.V.; Grigorieva, I.V.; Firsov, A.A. Electric field effect in atomically thin carbon films. *Science* **2004**, *306*, 666–669. [CrossRef]
16. Miura, Y.; Kasai, H.; Diño, W.; Nakanishi, H.; Sugimoto, T. First principles studies for the dissociative adsorption of H_2 on graphene. *J. Appl. Phys.* **2003**, *93*, 3395–3400. [CrossRef]

17. Durgun, E.; Ciraci, S.; Yildirim, T. Functionalization of carbon-based nanostructures with light transition-metal atoms for hydrogen storage. *Phys. Rev. B* **2008**, *77*, 085405. [CrossRef]
18. Liu, J.; Cui, L.; Losic, D. Graphene and graphene oxide as new nanocarriers for drug delivery applications. *Acta Biomater.* **2013**, *9*, 9243–9257. [CrossRef]
19. Davis, M.E.; Chen, Z.G.; Shin, D.M. Nanoparticle therapeutics: An emerging treatment modality for cancer. *Nat. Rev. Drug Discov.* **2008**, *7*, 771–782. [CrossRef]
20. Ibrahim, M.A.A.; Hamad, M.H.A.; Mahmoud, A.H.M.; Mekhemer, G.A.H.; Sayed, S.R.M.; El-Rahman, M.K.A.; Sidhom, P.A.; Dabbish, E.; Shoeib, T. On the use of graphene nanosheets for drug delivery: A case study of cisplatin and some of its analogs. *Pharmaceutics* **2023**, *15*, 1640. [CrossRef]
21. Ibrahim, M.A.A.; Hamad, M.H.A.; Mahmoud, A.H.M.; Mekhemer, G.A.H.; Sidhom, P.A.; Sayed, S.R.M.; Moussa, N.A.M.; Rabee, A.I.M.; Dabbish, E.; Shoeib, T. Adsorption of Favipiravir on pristine graphene nanosheets as a drug delivery system: A DFT study. *RSC Adv.* **2023**, *13*, 17465–17475. [CrossRef] [PubMed]
22. Palacios, J.J.; Fernandez-Rossier, J.; Brey, L. Vacancy-induced magnetism in graphene and graphene ribbons. *Phys. Rev. B* **2008**, *77*, 195428. [CrossRef]
23. Hou, Y.; Wen, Z.H.; Cui, S.M.; Ci, S.Q.; Mao, S.; Chen, J.H. An advanced nitrogen-doped graphene/cobalt-embedded porous carbon polyhedron hybrid for efficient catalysis of oxygen reduction and water splitting. *Adv. Funct. Mater.* **2015**, *25*, 872–882. [CrossRef]
24. Varghese, S.S.; Lonkar, S.; Singh, K.K.; Swaminathan, S.; Abdala, A. Recent advances in graphene based gas sensors. *Sens. Actuators B-Chem.* **2015**, *218*, 160–183. [CrossRef]
25. Zhang, S.; Yan, Z.; Li, Y.; Chen, Z.; Zeng, H. Atomically thin arsenene and antimonene: Semimetal-semiconductor and indirect-direct band-gap transitions. *Angew. Chem. Int. Ed. Engl.* **2015**, *54*, 3112–3115. [CrossRef]
26. Khan, A.F.; Randviir, E.P.; Brownson, D.A.C.; Ji, X.B.; Smith, G.C.; Banks, C.E. 2D hexagonal boron nitride (2D-hBN) explored as a potential electrocatalyst for the oxygen reduction reaction. *Electroanalysis* **2017**, *29*, 622–634. [CrossRef]
27. Zhang, S.; Xie, M.; Li, F.; Yan, Z.; Li, Y.; Kan, E.; Liu, W.; Chen, Z.; Zeng, H. Semiconducting group 15 monolayers: A broad range of band gaps and high carrier mobilities. *Angew. Chem. Int. Ed. Engl.* **2016**, *55*, 1666–1669. [CrossRef]
28. Aufray, B.; Kara, A.; Vizzini, S.; Oughaddou, H.; Leandri, C.; Ealet, B.; Le Lay, G. Graphene-like silicon nanoribbons on Ag(110): A possible formation of silicene. *Appl. Phys. Lett.* **2010**, *96*, 183102. [CrossRef]
29. Du, Y.; Zhuang, J.; Liu, H.; Xu, X.; Eilers, S.; Wu, K.; Cheng, P.; Zhao, J.; Pi, X.; See, K.W.; et al. Tuning the band gap in silicene by oxidation. *ACS Nano* **2014**, *8*, 10019–10025. [CrossRef]
30. Feng, B.; Zhang, J.; Zhong, Q.; Li, W.; Li, S.; Li, H.; Cheng, P.; Meng, S.; Chen, L.; Wu, K. Experimental realization of two-dimensional boron sheets. *Nat. Chem.* **2016**, *8*, 563–568. [CrossRef]
31. Mannix, A.J.; Zhou, X.F.; Kiraly, B.; Wood, J.D.; Alducin, D.; Myers, B.D.; Liu, X.; Fisher, B.L.; Santiago, U.; Guest, J.R.; et al. Synthesis of borophenes: Anisotropic, two-dimensional boron polymorphs. *Science* **2015**, *350*, 1513–1516. [CrossRef]
32. Ranjan, P.; Lee, J.M.; Kumar, P.; Vinu, A. Borophene: New sensation in flatland. *Adv. Mater.* **2020**, *32*, e2000531. [CrossRef]
33. Peng, B.; Zhang, H.; Shao, H.Z.; Xu, Y.F.; Zhang, R.J.; Zhua, H.Y. The electronic, optical, and thermodynamic properties of borophene from first-principles calculations. *J. Mater. Chem. C* **2016**, *4*, 3592–3598. [CrossRef]
34. Gao, M.; Li, Q.Z.; Yan, X.W.; Wang, J. Prediction of phonon-mediated superconductivity in borophene. *Phys. Rev. B* **2017**, *95*, 024505. [CrossRef]
35. Jiang, H.R.; Lu, Z.H.; Wu, M.C.; Ciucci, F.; Zhao, T.S. Borophene: A promising anode material offering high specific capacity and high rate capability for lithium-ion batteries. *Nano Energy* **2016**, *23*, 97–104. [CrossRef]
36. Tang, H.; Ismail-Beigi, S. Novel precursors for boron nanotubes: The competition of two-center and three-center bonding in boron sheets. *Phys. Rev. Lett.* **2007**, *99*, 115501. [CrossRef] [PubMed]
37. Yang, X.B.; Ding, Y.; Ni, J. Ab initio prediction of stable boron sheets and boron nanotubes: Structure, stability, and electronic properties. *Phys. Rev. B* **2008**, *77*, 041402. [CrossRef]
38. Li, W.L.; Jiang, Q.G.; Li, D.D.; Ao, Z.M.; An, T.C. Density functional theory investigation on selective adsorption of VOCs on borophene. *Chin. Chem. Lett.* **2021**, *32*, 2803–2806. [CrossRef]
39. Joshi, D.J.; Malek, N.I.; Kailasa, S.K. Borophene as a rising star in materials chemistry: Synthesis, properties and applications in analytical science and energy devices. *New J. Chem.* **2022**, *46*, 4514–4533. [CrossRef]
40. Ta, L.T.; Hamada, I.; Morikawa, Y.; Dinh, V.A. Adsorption of toxic gases on borophene: Surface deformation links to chemisorptions. *RSC Adv.* **2021**, *11*, 18279–18287. [CrossRef]
41. Liu, T.T.; Chen, Y.H.; Zhang, M.L.; Yuan, L.H.; Zhang, C.R.; Wang, J.; Fan, J.J. A first-principles study of gas molecule adsorption on borophene. *AIP Adv.* **2017**, *7*, 125007. [CrossRef]
42. Huang, C.S.; Murat, A.; Babar, V.; Montes, E.; Schwingenschlogl, U. Adsorption of the gas molecules NH_3, NO, NO_2, and CO on borophene. *J. Phys. Chem. C* **2018**, *122*, 14665–14670. [CrossRef]
43. Ibrahim, M.A.A.; Mahmoud, A.H.M.; Mekhemer, G.A.H.; Shawky, A.M.; Soliman, M.E.S.; Moussa, N.A.M. Adsorption behavior of toxic carbon dichalcogenides (CX2; X = O, S, or Se) on β12 borophene and pristine graphene sheets: A DFT study. *Nanomaterials* **2022**, *12*, 3411. [CrossRef] [PubMed]
44. Radilov, A.S.; Shkayeva, I.E.; Solntseva, S.A.; Kondrashov, V.A.; Menshikov, N.M.; Nikulin, O.S. Experimental studies of the toxic properties of halogen-derivatives of saturated hydrocarbons (Chladons). *Toxicol. Rev.* **2017**, 35–41. [CrossRef]

45. Agarwal, A.K.; Berndt, W.O.; Mehendale, H.M. Possible nephrotoxic effect of carbon tetrabromide and its interaction with chlordecone. *Toxicol. Lett.* **1983**, *17*, 57–62. [CrossRef]
46. Klingensmith, J.S.; Mehendale, H.M. Potentiation of CCl4 lethality by chlordecone. *Toxicol. Lett.* **1982**, *11*, 149–154. [CrossRef]
47. Babaa, M.R.; Dupont-Pavlovsky, N.; McRae, E.; Masenelli-Varlot, K. Physical adsorption of carbon tetrachloride on as-produced and on mechanically opened single walled carbon nanotubes. *Carbon* **2004**, *42*, 1549–1554. [CrossRef]
48. Bermudez, V.M.; Robinson, J.T. Effects of molecular adsorption on the electronic structure of single-layer graphene. *Langmuir* **2011**, *27*, 11026–11036. [CrossRef]
49. Li, K.; Li, N.; Yan, N.N.; Wang, T.Y.; Zhang, Y.T.; Song, Q.; Li, H.J. Adsorption of small hydrocarbons on pristine, N-doped and vacancy graphene by DFT study. *Appl. Surf. Sci.* **2020**, *515*, 146028. [CrossRef]
50. Chakarova-Kack, S.D.; Schroder, E.; Lundqvist, B.I.; Langreth, D.C. Application of van der Waals density functional to an extended system: Adsorption of benzene and naphthalene on graphite. *Phys. Rev. Lett.* **2006**, *96*, 146107. [CrossRef]
51. Ha, M.; Kim, D.Y.; Li, N.; Madridejos, J.M.L.; Park, I.K.; Youn, I.S.; Lee, J.; Baig, C.; Filatov, M.; Min, S.K.; et al. Adsorption of carbon tetrahalides on coronene and graphene. *J. Phys. Chem. C* **2017**, *121*, 14968–14974. [CrossRef]
52. Singh, D.; Kumar, A.; Kumar, D. Adsorption of small gas molecules on pure and Al-doped graphene sheet: A quantum mechanical study. *Bull. Mater. Sci.* **2017**, *40*, 1263–1271. [CrossRef]
53. Qin, G.Q.; Cui, Q.Y.; Du, A.J.; Sun, Q. Borophene: A metal-free and metallic electrocatalyst for efficient converting CO_2 into CH_4. *Chemcatchem* **2020**, *12*, 1483–1490. [CrossRef]
54. Bader, R.F.W.; Nguyen-Dang, T.T. Quantum theory of atoms in molecules–dalton revisited. In *Advances in Quantum Chemistry*; Löwdin, P.-O., Ed.; Academic Press: Cambridge, MA, USA, 1981; Volume 14, pp. 63–124.
55. Henkelman, G.; Arnaldsson, A.; Jonsson, H. A fast and robust algorithm for Bader decomposition of charge density. *Comp. Mater. Sci.* **2006**, *36*, 354–360. [CrossRef]
56. Kresse, G.; Furthmuller, J. Efficient iterative schemes for ab initio total-energy calculations using a plane-wave basis set. *Phys. Rev. B* **1996**, *54*, 11169–11186. [CrossRef]
57. Kresse, G.; Furthmuller, J. Efficiency of ab-initio total energy calculations for metals and semiconductors using a plane-wave basis set. *Comp. Mater. Sci.* **1996**, *6*, 15–50. [CrossRef]
58. Giannozzi, P.; Baroni, S.; Bonini, N.; Calandra, M.; Car, R.; Cavazzoni, C.; Ceresoli, D.; Chiarotti, G.L.; Cococcioni, M.; Dabo, I.; et al. QUANTUM ESPRESSO: A modular and open-source software project for quantum simulations of materials. *J. Phys. Condens. Matter* **2009**, *21*, 395502. [CrossRef] [PubMed]
59. Giannozzi, P.; Andreussi, O.; Brumme, T.; Bunau, O.; Buongiorno Nardelli, M.; Calandra, M.; Car, R.; Cavazzoni, C.; Ceresoli, D.; Cococcioni, M.; et al. Advanced capabilities for materials modelling with Quantum ESPRESSO. *J. Phys. Condens. Matter* **2017**, *29*, 465901. [CrossRef]
60. Perdew, J.P.; Burke, K.; Ernzerhof, M. Generalized gradient approximation made simple. *Phys. Rev. Lett.* **1996**, *77*, 3865–3868. [CrossRef]
61. Vanderbilt, D. Soft self-consistent pseudopotentials in a generalized eigenvalue formalism. *Phys. Rev. B* **1990**, *41*, 7892–7895. [CrossRef]
62. Grimme, S. Semiempirical GGA-type density functional constructed with a long-range dispersion correction. *J. Comput. Chem.* **2006**, *27*, 1787–1799. [CrossRef]
63. Marzari, N.; Vanderbilt, D.; De Vita, A.; Payne, M.C. Thermal contraction and disordering of the Al(110) surface. *Phys. Rev. Lett.* **1999**, *82*, 3296–3299. [CrossRef]
64. Kutzelnigg, W. Book review: Atoms in molecules. A quantum theory. (International Series Monographs on Chemistry, Vol. 22). By R. F. W. Bader. *Angew. Chem. Int. Ed. Engl.* **1993**, *32*, 128–129. [CrossRef]
65. Momma, K.; Izumi, F. VESTA 3 for three-dimensional visualization of crystal, volumetric and morphology data. *J. Appl. Crystallogr.* **2011**, *44*, 1272–1276. [CrossRef]
66. Andreussi, O.; Dabo, I.; Marzari, N. Revised self-consistent continuum solvation in electronic-structure calculations. *J. Chem. Phys.* **2012**, *136*, 064102. [CrossRef] [PubMed]